Latent Heat Fluxes Through Nano-engineered Porous Materials

For presentation at the June 2006 ASME Nano-Energy Conference, Cambridge, MA, and Simultaneous Submission to the *ASME Journal of Heat Transfer*

Matthew J. Traum[1,2,1], Peter Griffith[2], Edwin L. Thomas[1,3], and William A. Peters[1,2]

[1]Institute for Soldier Nanotechnologies,
Massachusetts Institute of Technology
NE47 – Fourth Floor
77 Massachusetts Avenue
Cambridge, MA 02139

[2]Department of Mechanical Engineering,
Massachusetts Institute of Technology
77 Massachusetts Avenue
Cambridge, MA 02139

[3]Department of Material Science and Engineering,
Massachusetts Institute of Technology
77 Massachusetts Avenue
Cambridge, MA 02139

Last Updated 5/26/2006

Abstract

Transport of high-latent-heat-content vapor through pores in soft materials gives rise to substantial energy fluxes without high temperature gradients. Thermal management in nano-structures, MEMS, and larger systems, e.g., protective clothing, are potential applications. To exploit these opportunities requires quantitative understanding of vapor mass transfer within porous structures at realistic heat loads, including size-related effects of smaller pores (10-10,000 nm) e.g., rarefaction and surface curvature. This paper presents measured rates of water vapor transport across fiber-on-end membranes of Nucrel® (and Hytrel®) of thickness 113-126 μm (113-123 μm), with straight through pores of diameter 1.2-1.4 μm (8.4-14.1 μm), and average overall porosity of 6% (11%). Detailed mass-transfer analysis and modeling for an apparatus capable of measuring mass flux rates through porous membranes is presented. The apparatus is capable of delivering water vapor at known mass concentrations in air to the upstream face of each membrane by controlled heating of liquid water from below at 1400 ± 70 W/m^2 (to mimic a typical daytime solar and metabolic heat load on desert soldiers). Steady state rates of vapor transport through the membrane to zero-humidity ambient air were quantified by continuously weighing the entire apparatus and correcting for boundary layer mass transfer downstream of the membrane. The results were compared with predictions from Fickian diffusion with radial variations in vapor concentration at the membrane entrance and boundary layer effects. An effective overall ratio of sensible to latent heat transfer incorporating physical membrane properties was deduced for each membrane.

[1] Presenting Author: mtraum@mit.edu
[2] Corresponding Author: peters@mit.edu

Introduction

We have previously shown that evaporative cooling by transport of latent heat across nano-engineered porous membranes can be utilized to enhance cooling of underlying surfaces[i]. The heat- and mass-transfer implications of membrane pore size and geometry on latent heat exchange merit additional study. Pore diameters of 10-10,000 nm are of interest because of potential applications to heat management in multi-functional nano-structures, MEMS and macro systems based thereon. "Nano-trusses" are polymeric materials whose ordered networks of micro- to nano-scale rods, struts, cells, and channels provide light-weight, high porosity, and extraordinary absorption of mechanical energy[ii]. Thus nano-trusses show promise for integrating blast and ballistic protection with evaporative cooling.

To isolate and study mass transfer through nano-trusses, we created a lab-bench-scale experiment for rapid testing of heat- and mass-transfer through porous membanes. A smooth copper surface inside the apparatus is heated from beneath at flux densities equal the estimated metabolic plus daytime solar thermal load on desert Soldiers (1400±70 Wt/m2). From the copper surface, the apparatus delivers water vapor at known mass concentrations in air to the upstream face of a membrane under study. Steady state rates of vapor transport through the membrane to zero-humidity nitrogen gas were quantified by continuously weighing the entire apparatus and correcting for boundary layer mass transfer downstream of the membrane.

This paper presents measured rates of water vapor transport across fiber-on-end membranes (FOEMs) of Nucrel® (and Hytrel®) of thickness 113-126 μm (113-123 μm), with straight through pores of diameter 1.2-1.4 μm (8.4-14.1 μm), and average overall porosity of 6% (11%). The results were compared with two models: 1) a lumped heat- and mass-transfer thermal model incorporating all thermal flows to facilitate a heat balance and 2) a Fickian diffusion model with corrections for radial variations in vapor concentration at the upstream membrane face entrance and boundary layer effects at the downstream membrane face. Both models showed good agreement with experimental data, indicating that enough understanding has been developed to extend the research to membranes with a full range of pore diameters from 10nm to 10,000nm.

Experimental Apparatus

An experimental apparatus, shown in Figure 1 and described previously[iii], was utilized to make diffusion measurements. Device assures that the largest resistance to water vapor diffusion occurs across the porous membrane sample under study, and it assures that steady state conditions persist long enough to obtain reliable heat- and mass-transfer data. The water vapor mass concentrations at the membrane upstream and downstream surfaces are deduced by temperature readings at those locations.

Buoyancy-driven natural convection in the water charge and the headspace air is critical for proper function of the evaporation chamber. The (thermal) Rayleigh numbers for these two fluids were calculated from data taken during an experiment with no membrane in place (so-called "open-chamber"). A steady state temperature difference of about 10.6°C was measured between the chamber bottom and the water-air interface using Omega 5SC-TT-T-40-36 T-type thermocouples. When the chamber has an initial 7.0-gram water charge, the calculated water Rayleigh number is about 1.4×10^6, where the Rayleigh number is defined as

$$Ra = \frac{gL^3 \beta \Delta T}{\nu \alpha} \qquad \text{(Equation 1)}$$

The water Rayleigh number is far above the critical value of 1101 for onset of free convection in a fluid confined by a solid boundary on the bottom and a free surface on top[iv]. Buoyancy-driven circulation within the water was observed experimentally using a tracer. As liquid water evaporates away during the experiment the water depth, L, decreases, which causes the water Rayleigh number to decrease. Assuming that L is the only

parameter that changes during evaporation, the water Rayleigh number remains above the critical value for natural convection until the water weight drops below 0.6 grams.

The Rayleigh number in the head space air atop the water is defined as in Equation 1 above, except the physical properties of water are replaced by those for air. A characteristic driving temperature difference was measured between the air-water interface and the upstream membrane face during a closed-chamber run. At the beginning of an FOEM experiment, the head space Rayleigh number is 1384, just below the critical value of 1708 for natural convection of a fluid confined by a solid boundary top and bottom[v]. However, as the water evaporates, the head space grows taller. The Rayleigh number increases to over 11,000 by the time the water is exhausted. The evaporation chamber was sized to assure the Rayleigh number in the head space surpasses the critical value well before steady-state conditions are achieved. Head space buoyancy drives the water vapor across the liquid-air interface and up the inside walls of the chamber. This flow "chirality" was observed experimentally using a water vapor tracer in an open-chamber experiment.

The stability analysis for buoyancy-driven flow in the head space assumes that the evaporation chamber is a control volume with constant mass. Since mass leaves the experimental system continuously through the membrane, the density of the air-water mixture near the chamber top is lower than the value assumed when calculating the driving concentration gradient for the Rayleigh number. This density difference could potentially change the stability analysis leading to the derivation of the critical head space Rayleigh number for circulation onset. However, at 41°C and 1 atmosphere, typical operating conditions at the upstream membrane face, dry air density is 1.12 kg/m^3 while saturated air density is 1.09 kg/m^3; a difference of only 2.7 percent[vi]. Since a comparably small amount of moisture is lost through the membrane, the impact on density must be much smaller than 2.7 percent and can be ignored in the critical Rayleigh number calculations.

Since buoyancy-driven convective flow is critical to the proper function of the evaporation chamber, the water Rayleigh number (which decreases as water evaporates) and the head space Rayleigh number (which increases as water evaporates) define the operating envelope for the apparatus. If the apparatus is functioning at steady-state temperature within this envelope, the mass flux through the membrane remains constant, as demonstrated experimentally in Figure 2. Due to buoyancy-driven convection, there is no water vapor diffusion resistance in the head space. This result is important because it shows that the experiment is unaffected by changing in water depth.

If heat transfer inside the evaporation chamber occurred purely by conduction, a majority of the input thermal energy would bypass the water and travel up the copper walls and out the top of the apparatus. However, natural convection in the water produces substantial convective heat transfer at the copper surface, causing a majority of the input heat to enter the water. For flow over the bottom chamber surface, the average Nusselt number correlation for natural convection on a heated horizontal plate facing up is[vii]:

$$\overline{Nu}_L = 0.54 Ra_L^{0.25} \qquad \text{(Equation 2)}$$

From one-dimensional heat-transfer modeling, the relative contributions to axial heat transmission into the bulk fluid by buoyant convection, conduction along the copper walls, and conduction through the liquid water are 69.3%, 26.7%, and 3.8% respectively. Importantly, over 70% of the input energy is transmitted directly through the water via natural convection and conduction. At most, 30% of the heat input would short-circuit the water if conduction through the copper walls were entirely one-dimensional.

Given the still-significant thermal short around the water, it may seem counter-intuitive to utilize a thermally-conductive copper-walled evaporation chamber instead of some low-conductivity material like Pyrex. In addition to simplifying the chamber fabrication, the copper walls play a crucial role in assuring that air fully-saturated with water vapor circulates in the head space. High-thermal-conductivity copper assures that the head space chamber walls are never cooler than the liquid-air interface. Therefore, liquid water cannot condense on

the chamber walls before circulating up to the membrane. The relative humidity on the upstream side of the membrane must be 100%, and the water concentration at that location can therefore be deduced from a temperature reading.

Mills[viii] gives a correlation for average Nusselt number from a laminar boundary layer on a vertical wall induced by natural convection:

$$\overline{Nu}_L = 0.68 + 0.670\left(Ra_L \left[1 + \left(\frac{0.492}{\mathrm{Pr}} \right)^{9/16} \right]^{-16/9} \right)^{0.25} \qquad \text{(Equation 3)}$$

Using the associated convection coefficient, a fin approximation model was developed for axial temperature gradient in the copper walls adjacent to the water charge. This model shows that the copper wall temperature at the air-water interface is hotter than the fluid, assuring that water vapor can not condense out of the air onto the head space walls. Therefore, air reaching the membrane must be water-saturated (or super-saturated) because the upstream membrane face temperature is cooler the liquid-air interface. During closed–chamber and FOEM experiments, water droplets were observed forming on the upstream membrane face, experimentally demonstrating that the head-space air is saturated at that location. If low-conductivity (i.e. Pyrex) chamber walls were used, water vapor would condense on the cooler walls before reaching the membrane, eliminating the ability to calculate water vapor species concentration at the upstream membrane surface with a single temperature measurement.

Formation of water droplets on the upstream membrane face might impact the thermal performance of the apparatus by allowing liquid water to wick through the membrane channels and emerge on the downstream membrane face where evaporation could occur. This additional transport mechanism would tend to artificially increase the system's effective cooling because sensible heat would be transported out of the control volume by wicking and the membrane would also experience additional cooling as the liquid water evaporated from the downstream membrane surface.

To check for wicking liquid water, a small piece of filter paper with mass known to ±1 mg was utilized. The filter paper was hung on a support within the lab 24 hours prior to the experiment to allow equilibration with the humidity in the room. The experimental apparatus was turned on and allowed to reach steady state during which visible water droplets formed on the upstream membrane face. The apparatus was then allowed to cool to room temperature to minimize the vapor diffusion through the membrane. The pre-weighed filter paper was raked across the downstream membrane face over the spots where water droplets on the upstream face were visible. The paper's weight after raking was found to be unchanged within the sensitivity of the scale, demonstrating that liquid water was not wicking up through the membrane pores.

Apparatus Modeling

There are several mechanisms through which mass transfer could occur across the membrane: thermal transpiration, Stefan flow, and diffusion. Analyses were performed to eliminate transpiration and Stefan flow as significant contributions, leaving diffusion as the only major mass transport mechanism.

Diffusion resistances encountered by the water vapor as it leaves the evaporation chamber were modeled to estimate the expected mass flux. There are two significant diffusion resistances: the porous membrane itself and the boundary layer created at the membrane downstream face by dry nitrogen blown over the surface. The electrical analogy of two resistors in series is used to model mass transport. The membrane mass transfer resistance is

$$R_{mem} = \frac{l\tau}{D_{ab}\varepsilon} \quad \text{(Equation 4)}$$

For the representative case of Nucrel A, R_{mem} = 80.7 s/m. Summing the membrane resistance with the boundary-layer-based diffusion resistance yields the complete mass transfer expression,

$$\dot{m} = \frac{A}{R_{mem} + R_{BL}}\left(-\rho_{a,1}\right) \quad \text{(Equation 5)}$$

The following sections explain refinements for R_{mem} that correct for buoyancy-driven circulation in cylindrical geometry within the evaporation chamber. Methods to find bounding values on R_{BL} are also outlined.

One-Dimensional Fick's Law Model

The simplest method to estimate mass flux through the FOEMs is to apply Fick's Law for one-dimensional diffusion, treating the membrane as a bottleneck resistance to diffusion. When written in terms of mass flux, $\dot{m}$, Fick's law in one dimension is

$$\dot{m} = \frac{D_{ab}A\varepsilon}{\tau L}\left(\rho_{a,2} - \rho_{a,1}\right) \quad \text{(Equation 6)}$$

Based on FOEM characterization using scanning electron microscopy[ix], the porosity, tortuosity, and thickness of each sample was established. Since the pores are open to the ambient air on both sides, the diffusion coefficient, D_{ab}, is calculated for water vapor diffusing through air[x],

$$D_{H_2O,air} = 1.87\times10^{-10}\frac{T^{2.072}}{P} \quad \text{(Equation 7)}$$

The correlation temperature is the average between the upstream and downstream face temperatures of the membrane, measured experimentally. The pressure is one atmosphere, plus a small correction to account for the presence of water vapor. For the representative case of Nucrel A, D_{ab} is 2.54 x 10^{-5} m^2/s for an average membrane temperature of 310.2 K. This result compares favorably with an experimental value reported in Deen[xi] of 2.59 x 10^{-5} m^2/s at 308 K and one atmosphere for water vapor diffusing in nitrogen.

The water vapor mass concentrations at the upstream face and downstream faces of the membrane are found using the ideal gas law and the relative humidity at each station. At the downstream face, dry nitrogen blows over the surface of the membrane, effectively making the relative humidity (and the water mass concentration) zero. At the upstream face, the water concentration, $\rho_{a,1}$, can be determined from

$$\rho_{a,1} = \frac{m}{V} = \frac{M \cdot P_{water}}{R_U \cdot T} \quad \text{(Equation 8)}$$

A table of the thermodynamic properties for saturated steam[xii] is utilized to estimate the saturation pressure of water vapor at the temperature of the upstream membrane face.

Radial Concentration Gradient

Alone, the one-dimensional Fick's Law model over-predicts the mass flux across the membrane because it does not account for the two-dimensional impact of buoyancy-driven circulation on the radial concentration gradient at the upstream membrane face.

Figure 3 shows a schematic representation of circulation in the head space. Convection cells circulate water-vapor-rich air from the liquid-air interface up the evaporation chamber wall to the upstream membrane face. The circulation cell then moves the saturated fluid radially inward across the membrane toward the chamber's center. As the fluid moves, water vapor diffuses through the membrane, reducing the water vapor concentration in the circulation cell as it progresses from the outer radius to the center.

To quantify the resulting radial concentration gradient, a differential equation was developed for a characteristic elemental fluid element. The element is a torus at radius r from the center of the membrane.

$$\frac{\partial \rho}{\partial t} = -\Lambda A \rho \qquad \text{(Equation 9)}$$

Due to the cylindrical geometry of the evaporation chamber, all variables of interest in Equation 9 are functions of radius. So, a numerical solution approach is warranted. Water vapor mass concentration continuity is cast into a form competent for numerical integration.

$$\rho(r+dr)dV = \rho(r)dV - \frac{dm}{dt}\cdot\Delta t \qquad \text{(Equation 10)}$$

Using Taylor expansion on the left hand side of this expression and converting from time to spatial coordinates, an exact index expression for the water vapor mass concentration inside the characteristic fluid element is obtained, taking the limit as dr approaches zero:

$$d\rho = -\frac{1}{V}\left(\frac{dm}{dt}\right)\cdot\frac{dr}{dU} \qquad \text{(Equation 11)}$$

The boundary condition is the water vapor mass concentration at the outside radius of the membrane defined by the ideal gas law and the upstream temperature of the membrane. By selecting an appropriately small step in radius, dr, the radius-dependant variables can be solved at each step. The process is iterated until r reaches the center of the membrane, resulting in a precise water vapor mass concentration as a function of radial position.

Applying mass continuity to the representative fluid element, the flow velocity must increase as the fluid approaches the center of the membrane because the available cross-sectional flow area drops. It is assumed that the fluid's density change due to mass flux across the membrane can be neglected. The initial boundary velocity at the outer radius must be determined to compute Equation 9 numerically. Deen[xiii] derives a characteristic velocity for buoyancy-driven natural convection,

$$U_b = \left(gL\beta\Delta T\right)^{0.5} \qquad \text{(Equation 12)}$$

Substituting characteristic values into Equation 10 for the evaporation chamber at the beginning of the steady-state period gives U_b = 0.095 m/s. As the water in the evaporation chamber is depleted, the characteristic velocity increases; by the time the experiment has lost enough water to leave the steady-state operating envelope, U_b = 0.128 m/s. Therefore, an average value of U_b = 0.112 m/s is utilized for calculating $\rho(r)$.

As an experimental check on U_b, videos were taken during an open-chamber experiment using a tracer to visualize the speed of convective circulation. The approximate tracer velocity was 0.05 m/s, about 45 % of the calculated characteristic velocity.

The characteristic fluid element volume is the product of differential area, dA, and some characteristic height, h. The resulting $\rho(r)$ depends on the value selected for h. The boundaries of the characteristic fluid element are the membrane on the top and an imaginary boundary on the bottom through which no mass can travel. The bottom edge is well-approximated by a viscous boundary layer.

As shown in Turner[xiv], natural convection cells move with rapid circulation that increases towards the center of the cells. Inside the evaporation chamber, mixing within the circulation cells assures that most of the bulk air in the head space is nearly saturated with water vapor. However this water-vapor-rich air cannot convect into viscosity-dominated boundary layer near the membrane. Water vapor can only readily pass into the boundary layer by diffusion. Diffusion mass flux is driven by concentration gradient, and the concentration gradient across the upstream membrane face boundary layer is small compared with the concentration gradient across the membrane. The mass of water vapor migrating into the boundary layer is therefore small compared to the amount leaving, and for the purposes of modeling, the boundary layer represents a border across which mass cannot pass. The boundary layer height is used to estimate the height of the characteristic fluid element. The assumption of small mass concentration gradient across the boundary layer will be proven by calculating $\rho(r)$ and comparing it to the saturation water vapor concentration within the evaporation chamber. It will be shown that water vapor migration into the boundary layer is negligible compared to mass diffusion through the membrane.

The flow velocity creating the upstream membrane face boundary layer originates due to natural convection. However, a Rayleigh number correlation is not the correct way to determine the membrane boundary layer thickness because the flow can no longer move upward under buoyant forces once it reaches the membrane. Since the characteristic velocity of the flow is known, a Reynolds number can be calculated and the boundary layer thickness approximated using the Blasius solution for flow over a flat plate.

$$h(r) = \frac{5r}{\mathrm{Re}_r^{0.5}} \qquad \text{(Equation 13)}$$

Continuity in the cylindrical space forces the velocity of the flow to increase toward the center of the membrane. Therefore, the radial position, r, appears in the Reynolds number both as a pure variable and in its influence on velocity

$$\mathrm{Re}_r = \frac{\rho_{air} \cdot V(r) \cdot r}{\upsilon} \qquad \text{(Equation 14)}$$

While the geometry and conditions of this boundary layer formation are dissimilar to those under which the Blasius solution was derived, the Blasius solution nonetheless represents a computationally inexpensive means to estimate the boundary layer height to the correct order or magnitude. A rough approximation of the boundary layer thickness is adequate because the numerical integration for $\rho(r)$ is relatively insensitive to h(r). For example, the water vapor concentration at the membrane center, $\rho(r=0)$, which is the location most sensitive to changes in the model, increased by only 17.1% for an over-predication of 10 times in h(r). Therefore, the Blasius solution is deemed adequate to obtain reasonable model results.

Equations 9 and 11 are implemented numerically in MATLAB to calculate $\rho(r)$. With the radial concentration gradient known, the modeling assumptions made above can be checked. Does the viscous boundary layer on the upstream membrane face represent a virtual border to mass transfer? Fick's Law was applied between the bulk head space air (assumed to be saturated) and the boundary layer concentration, $\rho(r)$, using the representative boundary layer thickness, h(r) as the diffusion resistance length. For the representative case of Nucrel A with a fluid particle dwell time of 0.128 seconds (calculated using R/U_b), 8.3×10^{-8} kg of water vapor leaves the characteristic fluid element while only 1.1×10^{-8} kg enters during the time it is in contact with the membrane.

The source term is only 13 percent of the sink term, indicating that the viscous boundary layer can be used as a representative characteristic fluid particle height for purposes of modeling.

Membrane Downstream Face Boundary Layer

The second significant resistance to diffusion occurs due to the boundary layer, which forms on the downstream face of the membrane resulting from the dry nitrogen blown across this surface at 2.8 ± 0.25 m/s. The condition (laminar or turbulent) of the nitrogen flow is critical for proper modeling of the boundary layer. Experimental data indicate that the boundary layer is turbulent.

The tube carrying the nitrogen to the experimental apparatus is 6.67mm in diameter, and the flow is assumed to be at room temperature when exiting the nozzle. From these parameters, the Reynolds number for internal flow is calculated to be 1201, well below $Re_D < 2300$ for the onset of turbulence. However, as no diffuser was used at the tube's end, there is a sharp transition between tube flow and jet flow.

After jetting from the nozzle, the flow develops along the Styrofoam insulation collar for about 77 mm before reaching the membrane. The Styrofoam collar is extremely rough, with spheroids on the order of a 1.5 to 2.5 millimeters protruding from the surface in a vaguely hexagonal pattern. In this region, a flat plate flow model is used. If the plate were smooth, the Re_L when the flow reaches the membrane would be 12,181; below the accepted transition threshold for turbulent flow over a flat plate, $Re_{L,tr}$ = 300,000. Nonetheless, the sharp transition from pipe flow to jet flow to flow over a flat plate coupled with the surface roughness of the Styrofoam collar induces growth of turbulent boundary layer. Experimentally, turbulent eddies are seen forming ahead of the membrane on the Styrofoam collar (Fig. 4) using a tracer mixed with the nitrogen gas.

The Sherwood number for turbulent boundary layer development over a flat plate was utilized to provide an upper bound on boundary layer mass transfer resistance[xv],

$$\overline{Sh}_{turb} = \frac{H_{BL,turb} L}{D_{12}} = \int_{L_o}^{L_f} \frac{0.0296\left(\frac{u_e x}{\upsilon}\right)^{\frac{4}{5}} Sc}{x\left\{1 + 12.7\left[.0296\left(\frac{u_e x}{\upsilon}\right)^{\frac{-1}{5}}\right]\cdot\left[Sc^{\frac{2}{3}} - 1\right]\right\}} dx \qquad \text{(Equation 15)}$$

This equation is valid for $0.5 < Sc < 2000$ and $10^5 < Re_x < 10^7$. Despite low Reynolds number ($Re_x = 1.2x10^4$), this correlation was elected for modeling to capture the experimentally observed turbulent nature of the flow. Integrating equation 15 for the representative case of Nucrel A, the resulting Sherwood number is $\overline{Sh}_{turb}$ = 14.56 and $R_{BL,SH}$ = 76.6 s/m.

A lower bound approach to modeling the boundary layer resistance is to rely upon fluid dynamics to estimate relevant boundary layer heights. The turbulent boundary layer includes a very thin region in the vicinity of the wall called the viscous sub-layer. The bulk turbulent boundary layer is characterized by turbulent eddies that induce significant fluid mixing between the boundary layer and the ambient fluid. Since the ambient fluid is the dry nitrogen jet, the humidity in the bulk portion of the boundary layer approaches zero. However, in the viscous sub-layer, the flow is dominated by viscous forces; turbulent mixing and convection cannot occur. Therefore, this region is capable of supporting a water vapor concentration gradient between the upstream face of the membrane and the bulk turbulent boundary layer. The concentration gradient in the viscous sub-layer is assumed to be linear, a good approximation considering the extreme thinness of the layer and the linear nature of the velocity profile within it. The viscous sub-layer can therefore be treated as a diffusion resistance.

Prandlt's "Law of the Wall" states that in the region near a solid boundary the turbulent boundary layer velocity profile is described by a dimensionless linear expression,

$$u^+ = \frac{U}{u_\tau} = \frac{\delta u_\tau}{\upsilon} = y^+ \qquad \text{(Equation 16)}$$

The friction velocity, u_τ, is determined from the sheer stress on the wall[xvi]:

$$u_\tau(x) = U\left(\frac{C_{f,x}}{\rho}\right)^{1/2} \qquad \text{(Equation 17)}$$

There are three turbulent regimes of wall skin friction: 1) smooth surface, which depends only on Re; 2) rough surface, which depends only on the ratio of surface roughness to plate length; and 3) transition, which depends on both Re and surface roughness. Due to the irregularity of surface features on the Styrofoam collar over which the flow passes on its way to the membrane, it is impossible to calculate the surface roughness based on the standard Nikuradse sand roughness[xvii]. However, the membrane itself approximates a smooth surface, a representative bounding case for which a skin friction correlation exits[xviii],

$$C_{f,x,smooth} = 0.0592 \cdot \mathrm{Re}^{\frac{-1}{5}} \qquad \text{(Equation 18)}$$

This correlations is valid for $10^5 < \mathrm{Re} < 10^7$, but it is nonetheless utilized for this situation in which $\mathrm{Re} = 1.2\text{x}10^4$. Equation 16 only applies within the viscous sub-layer. Beyond this region, the relationship between u^+ and y^+ is no longer linear. The linear viscous sub-layer region exists between $0 < y^+ < \delta^+$ where δ^+ is about 5[xix]. Plugging Equations 17 into Equation 16 and re-arranging for $\delta(x)$ gives:

$$\delta(x)_{smooth} = \frac{5\upsilon}{U\left(\frac{C_{f,x,smooth}}{\rho}\right)^{1/2}} \qquad \text{(Equation 19)}$$

To find the average viscous sub-layer thickness over the membrane, we integrate over the membrane length,

$$\bar{\delta}_{smooth} = \frac{1}{L_f - L_o}\int_{L_o}^{L_f} \frac{5\upsilon}{U\left(\frac{C_{f,x,smooth}}{\rho}\right)^{1/2}}\,dx \qquad \text{(Equation 20)}$$

By dividing the average viscous sub-layer height by the diffusion coefficient of water vapor in air, a mass transfer resistance with proper units [s/m] results. For the representative case of Nucrel A, $\bar{\delta}_{smooth} = 4.0\text{x}10^{-4}$ m, and the associated diffusion resistances is $R_{BL,VSL} = 15.6$ s/m.

Experimental Procedure

The typical procedure was to thermally equilibrate de-ionized water to the ambient temperature by storing it in a covered graduated cylinder on the lab bench overnight. The evaporation chamber was weighed and then filled with ca 7.0 g of the equilibrated DI water giving a roughly 11-mm-deep charge. The chamber was then reweighed to determine the exact initial weight of the water. Except in positive control runs (i.e. no covering), the top opening of the evaporation chamber was then completely covered with a membrane sealed taught to the chamber outside wall by an elastic band. The insulation collar was forced over the chamber, and the entire

assembly was then placed on the heater and taped down to assure good thermal contact between the heater plate and the evaporation chamber bottom. A continuous flow of dry nitrogen gas was directed over the top of the apparatus (Fig. 1) from a tube at an exit velocity of 2.8 ± 0.25 m/s to match the rate utilized elsewhere[xx] for measuring the rate of vapor transmission rate through textiles. The tube exit velocity was measured using a VWR Enviro-Meter digital anemometer. The chamber bottom was then heated at 1400 ± 70 W_t/m^2 by manually adjusting a 110-volt-input, variable transformer (Variac) which powered an 85.55 mm OD ProvoCraft® Candlsense[tm] electrical hot plate (stated maximum heat flux density 3600 W_t/m^2). The experiments consisted of 4 runs with the latex membrane (negative control), 4 with no covering (positive control, i.e., maximum evaporative cooling) and 2 each with replicate samples of Nucrel® and Hytrel® from the same lot. Temperature and weight measurements were recorded every two minutes throughout each experiment.

When the evaporation chamber is initially placed on the heater, the electricity is not turned on. An alternative procedure used in earlier test runs allowed the heater to warm to steady-state temperature for about an hour before placing the evaporation chamber atop the heater. This earlier procedure has the advantage of assuring no radial thermal temperature gradients in the heater during the experiment's warm-up period. However, this alternative approach was ultimately abandoned because the heater was too hot to handle at steady-state temperature and the evaporation chamber could not be safely secured to the hot plate without spilling the water.

Once the evaporation chamber is affixed to the hot plate using the revised procedure, experimental time is started and allowed to run for 10 minutes before electricity is engaged. This delay provides data about the initial conditions of the evaporation chamber prior to the experiment. At time = 10 minutes, the electricity is turned on, and the system heats up. This approach requires that the entire heater be lumped into the thermal model.

After roughly 40 minutes, the system reaches steady-state conditions. Steady state is defined by two conditions: 1) the apparatus base temperature reading within 10% of the eventual average steady-state temperature and 2) adequate evaporation of water assures bouncy-driven natural convection is occurring in the head space. Since the average steady-state temperature can only be determined after the experiment, the exact time the experiment meets the steady-state criteria can only be determined by post-experimental review of the data.

The experiment runs in steady state for approximately 150 minutes or until less than 1 gram of liquid water remains in the evaporation chamber. The electricity is turned off and the system is allowed to cool. Data recording continues until the base temperature is within 10% of the ambient temperature.

Experimental Results

Figure 2 shows the time-rate-of-change for the evaporation chamber from the four FOEM runs of interest. The data has been normalized so that time = 0 represents the first data point taken when the experiment attains steady-state. The normalized weight is the apparatus weight subtracted from the weight of the system at the moment steady-state is achieved. Normalized weight loss is therefore reported as having a positive slope even through the apparatus weight drops as time moves forward.

Linear trend lines are plotted against the data for all four FOEM runs, and a linear fit to the data is computed, as shown in Figure 2. The strong data correlation to the linear trends shows that the experimental mass time-rate-of-change is a constant, indicating that the water vapor diffusion rate out of the evaporation chamber is also constant. This result is significant because it confirms the modeling assumption that mass transfer in the head space is facilitated by buoyancy driven natural convection. If pure diffusion through the head space were a significant bottleneck to water vapor transport, the mass transfer rate for the system would decrease as water evaporated away because the air head space diffusion length would grow as the water was depleted. Growing head space would correspond to increased diffusion resistance, which would slow mass transfer out of the system as time progressed.

By measuring the weight change of the apparatus under steady state conditions, the water vapor mass flux through the FOEM is determined. This mass flux can then be compared to the expected Fickian diffusion based on the species concentration on either side of the membrane to model and quantify the impact of the membrane on mass transfer.

Discussion

Validation of Mass Transfer Balance

Previously, we developed a heat- and mass-transfer model for the apparatus, Equation 21, which was validated by comparison with experimental results[xxi]. In a steady state heat balance for the FOEM runs (evaporation enabled), Equation 21 accounted for mass transfer to within +3.5-12.4%, as shown in Table 1.

$$C_p \cdot \frac{d(M \cdot T_1)}{dt} = \dot{Q}_{in} - Ah_{lumped}(T_1 - T_{amb}) - \dot{m} \cdot \mathrm{H}_{fg} \qquad \text{(Equation 21)}$$

Close heat balance agreement between the thermal model and the experimentally observed mass flux provides additional verification for the measured mass flux values.

Comparison of Diffusion Model to Experiment

Results of the diffusion mass-transfer models described above are represented in Figure 5 for the four FOEM runs. These results are compared with experimentally-measured flux rates for each case. In three cases, the models incorporating all major diffusion resistance effects (i.e. membrane resistance, radial concentration gradient, and boundary layer diffusion resistance) provide good agreement with experimental results. Nucrel B proves to be an anomaly. This sample had lower porosity and higher thickness than all the other samples, properties that should retard mass transport. Nonetheless, its measured mass flux was higher than all the other samples. (I am going to re-run the SEMs for Nucrel B to confirm the pervious characterization)

Comparison of Mass Flux to Human Sweat Rates

In their study of cooling options for the dismounted Soldier, Nellis, et al.[xxii] illuminate evaporative cooling as an attractive mechanism for soldier thermal management in desert conditions. Sweating, a natural form of evaporative cooling, is the principle mechanism for thermal regulation of the human body when ambient temperature exceeds internal body temperature. Schmidt-Nielsen[xxiii] reports typical desert sweating rates for human males in the range between 0.5 and 1.5 liters per hour. Assuming that the human body contains between 1 to 2 m^2 of surface area and that sweat is generated uniformly over the body, men must generate and evaporate between 0.25 to 1.5 kg/m^2 of water per hour for desert thermal management.

The experimental heat flux input of 1400 ± 70 W_t/m^2 was selected to mimic the combined daytime solar and metabolic heat load on desert Soldiers. Under this load, the FOEMs allow a mass flux of 0.30 to 0.38 kg/m^2-hour, an appreciable fraction of the human sweat rate for desert thermal management. This result represents a substantial improvement over existing soldier body armor, which affords almost no evaporative mass transfer. Despite their low total porosity (5-15%) and tiny pore sizes (as low as 1.2 μm), nano-engineered porous overlays show potential for integration of evaporative cooling with other useful capabilities, e.g., light weight, mechanical strength, and ballistic or blast protection, at realistic heat burdens and with appreciable solid material remaining for further tooling and massing functionality.

Derivation of Descriptive Ratio

To develop an appropriate dimensionless correlation that characterizes diffusion-enabled heat transfer through a porous membrane, the Buckingham-Pi theorem is applied. Eight independent parameters are identified: w, ΔT,

r, k, H_{fg}, $\Delta\rho$, ε/τ, and D_{12}. Of these parameters, four independent repeating variables are selected through which all dimensions of interest can be obtained: w [length], ΔT [temperature], $\Delta\rho$ [mass/legnth^3], and D_{12} [length^2/time]. With eight parameters and four repeating variables, the total number of dimensionless parameters is four. Expressing each variable in terms of its dimensions allows the Pi terms to be written explicitly:

$$\Pi_1 = \frac{r}{w} \quad \Pi_2 = \frac{k\Delta T w^2}{\Delta\rho D_{12}{}^3} \quad \Pi_3 = \frac{H_{fg} w^2}{D_{12}{}^2} \quad \Pi_4 = \frac{\varepsilon}{\tau} \qquad \text{(Equation 22)}$$

The product of two Pi terms yields the membrane ratio, ξ. This dimensionless number characterizes the contribution of physical membrane features to transport[xxiv], and its emergence is an indication that the choice of independent parameters was correct:

$$\xi = \frac{r\varepsilon}{t\tau} \quad \text{and} \quad \Pi_1 \cdot \Pi_4 = \frac{r\varepsilon}{t\tau} \qquad \text{(Equation 23)}$$

Interestingly, the Pi terms can also be combined to provide a result identical to an intuitively-derived descriptive dimensionless parameter for this system, the ratio of sensible heat transport to latent heat transport:

$$\frac{Q_{sens}}{Q_{lat}} = \frac{\frac{Ak}{L}\cdot\Delta T}{\frac{DA\varepsilon}{\tau L}\cdot\Delta\rho\cdot H_{fg}} = \frac{k\Delta T\tau}{D\Delta\rho H_{fg}\varepsilon} \text{ and } \frac{\Pi_2}{\Pi_3\cdot\Pi_4} = \frac{k\Delta T\tau}{D\Delta\rho H_{fg}\varepsilon} \qquad \text{(Equation 24)}$$

The sensible heat carried across the membrane in the heated water vapor can also make an appreciable contribution to the total energy transported, especially if the water vapor is super-heated vapor. At temperatures of interest for this study, however, the sensible heat contribution is small compared to the magnitude of transported latent heat. For example, to raise liquid water from room temperature, 30°C, to the evaporation chamber operating temperature, about 65°C, requires a heat input of about 147 kJ/kg. The latent heat associated with water vapor at 65°C is 2346 kJ/kg. The ratio of these two terms is the Jakob number, Ja = 0.0627, which indicates that only 5.9 percent of the energy carried by the diffusing species is in the form of sensible heat. The sensible heat contribution can therefore be ignored in the current analysis.

From the meteorology literature, the parameter obtained in Equation 24 can be identified as the Bowen ratio[xxv]. This parameter is also applicable as an engineering correlation, defining the ratio of sensible heat to latent heat transport across a membrane. For purely conductive problem, B approaches infinity, and for a purely diffusive problem, B approaches zero. Table 2 gives the Bowen ratios for each experimental FOEM test. The table shows that one tenth to one quarter of the heat leaving the system is transported as latent heat carried by water vapor diffusion.

Interestingly, energy transport by diffusion enables the possibility of moving energy across a boundary when no temperature gradient is present. Under a species mass concentration gradient, latent heat can be moved through membrane pores bound in vapor of the diffusion species. Importantly, diffusion also allows latent heat energy to move against temperature gradients, which is the case of interest for a soldier in the desert. The soldier can maintain a body temperature of 37°C when the environment is 50°C, provided there is a water vapor concentration gradient between his skin and the ambient environment to carry away energy as latent heat through evaporation. When sensible and latent heat transfer occur in opposing directions, the Bowen Ratio is negative.

Conclusions

Evaporative cooling by transport of latent heat across nano-engineered porous membranes can be utilized to enhance cooling of underlying surfaces. Nano-trusses provide light-weight, high porosity, and extraordinary absorption of mechanical energy, which make them interesting candidates of study for integrating blast and ballistic protection with evaporative cooling.

An experimental apparatus was developed for rapid testing of transport though nano-trusses at energy flux densities equal the estimated metabolic plus daytime solar thermal load on desert Soldiers. This device was tested using DuPont Nucrel® and Hytrel® FOEMs with straight through pores of diameter 1.2-1.4 μm (8.4-14.1 μm). This apparatus was verified using a lumped heat- and mass-transfer thermal balance model and a Fickian diffusion model with corrections for radial concentration and boundary layer effects. Both models showed good agreement with experimental data, indicating that enough understanding has been developed to extend the research to overlays with a full range of pore diameters from 10nm to 10,000nm.

Finally, a dimensionless parameter accounting for sensible and latent heat transport was derived. This parameter, recognized as the Bowen ratio from metrology, can be utilized to characterize the relative contributions of sensible and latent energy transfer in porous media thermal transport problems. Interestingly, latent heat transport via diffusion allows the transport of heat energy when no thermal gradient exists, corresponding to a Bowen ratio of zero. Of practical interest to the dismounted soldier, diffusion latent heat transport also allows heat energy to be moved against a thermal gradient, a situation for which the Bowen ratio is negative. This case has practical application in the desert where a soldier can maintain body temperature below ambient temperature by sweating through porous body armor fabricated using nano-trusses for combined ballistic protection and thermal management.

Acknowledgements

This research was supported by the U.S. Army through the Institute for Soldier Nanotechnologies, under Contract DAAD-19-02-D-0002 with the U.S. Army Research Office. The content does not necessarily reflect the position of the Government, and no official endorsement should be inferred. We acknowledge Dr. Ludowic Noels for consulting on the development of our numerical modeling techniques. We thank Drs. Vivek Kapur and Wayne Marsh of DuPont for supplying samples of their FOEM membranes. Hytrel® and Nucrel® are registered trademarks of the I. E. DuPont de Nemours Company.

Nomenclature

A: area
B: Bowen ratio
$C_{f,x}$: local skin friction at the wall
C_pM: apparatus thermal mass
D_{ab}: diffusion coefficient of species a in species b
dr: infinitesimal thickness
g: gravitational constant
h(r): boundary layer height as a function of radius
h: height
h_{lumped}: lumped convective heat transfer coefficient
H_{fg}: latent heat of vaporization
k: thermal conductivity
L: height of the water column
m: mass flux
M: molar mass
Nu: Nusselt number
Nu_L: Average Nusselt number based on length L
P: pressure

Pr: Prandlt number
P_{water}: partial pressure of water vapor
Q_{in}: heat input into the apparatus
r: radius
Ra_L: Rayleigh number based on length L
$R_{BL,SH}$: boundary layer diffusion resistance calculated using the Sherwood number
$R_{BL,VSL}$: boundary layer diffusion resistance calculated from the viscous sub-layer
R_{BL}: diffusion resistance arising form the downstream membrane boundary layer
Re_r: Reynolds number as a function of radius
R_{mem}: diffusion resistance arising form the membrane
R_u: universal gas constant
Sc: Schmidt number
Sh: Sherwood Number
T: temperature
U: free stream velocity
u^+: dimensionless velocity
U_b: characteristic velocity for buoyancy-driven natural convection
u_τ: friction velocity
w: membrane thickness
y^+: dimensionless boundary layer thickness

β: thermal expansion coefficient of liquid water
α: the thermal diffusivity of water
δ: boundary layer thickness
ΔT: thermal gradient
Δρ: concentration gradient
ε: membrane porosity,
Λ: Catch-all diffusion resistance parameter
ν: kinematic viscosity
ξ: membrane ratio
ρ_{air}: air density
ρ(r): water mass concentration as a function of radius
$\rho_{a,1}$: mass concentrations of species a at station 1
τ: membrane tortuosity

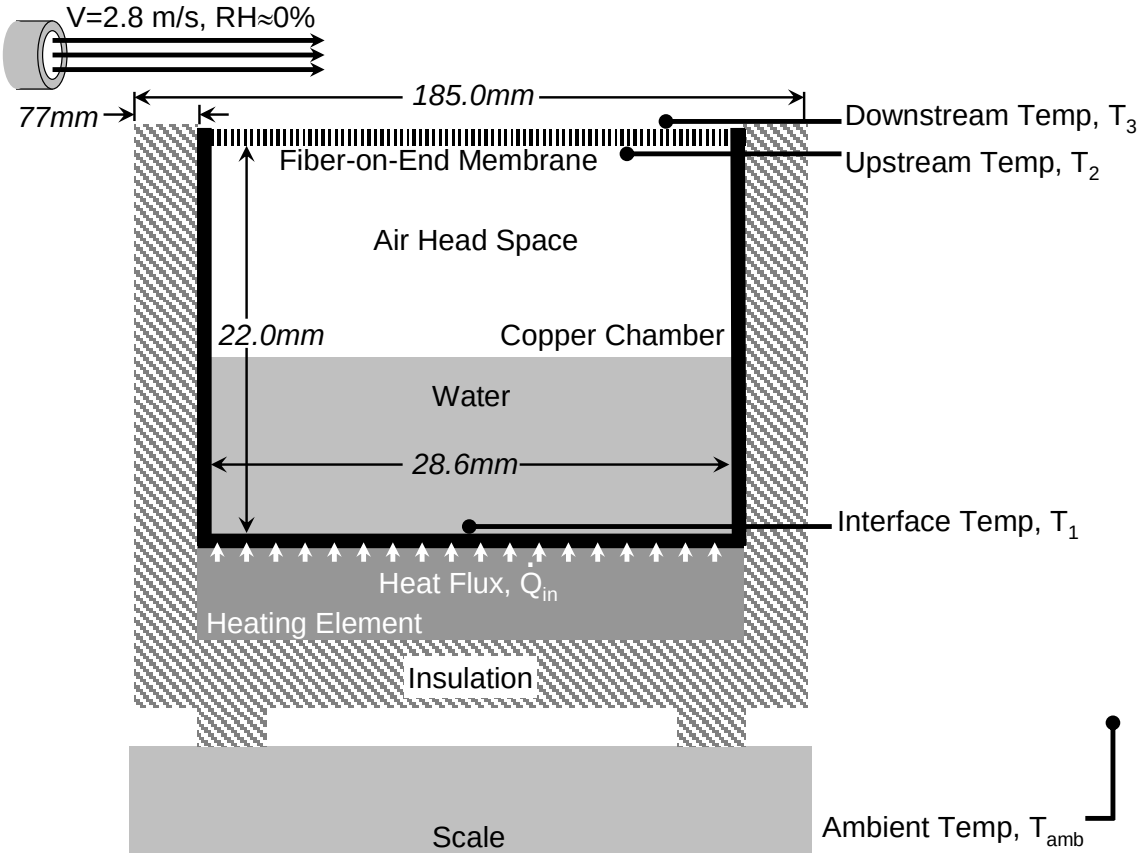

Figure 1: Schematic [not to scale] of apparatus for quantitative study of evaporative cooling of surfaces using porous overlays.

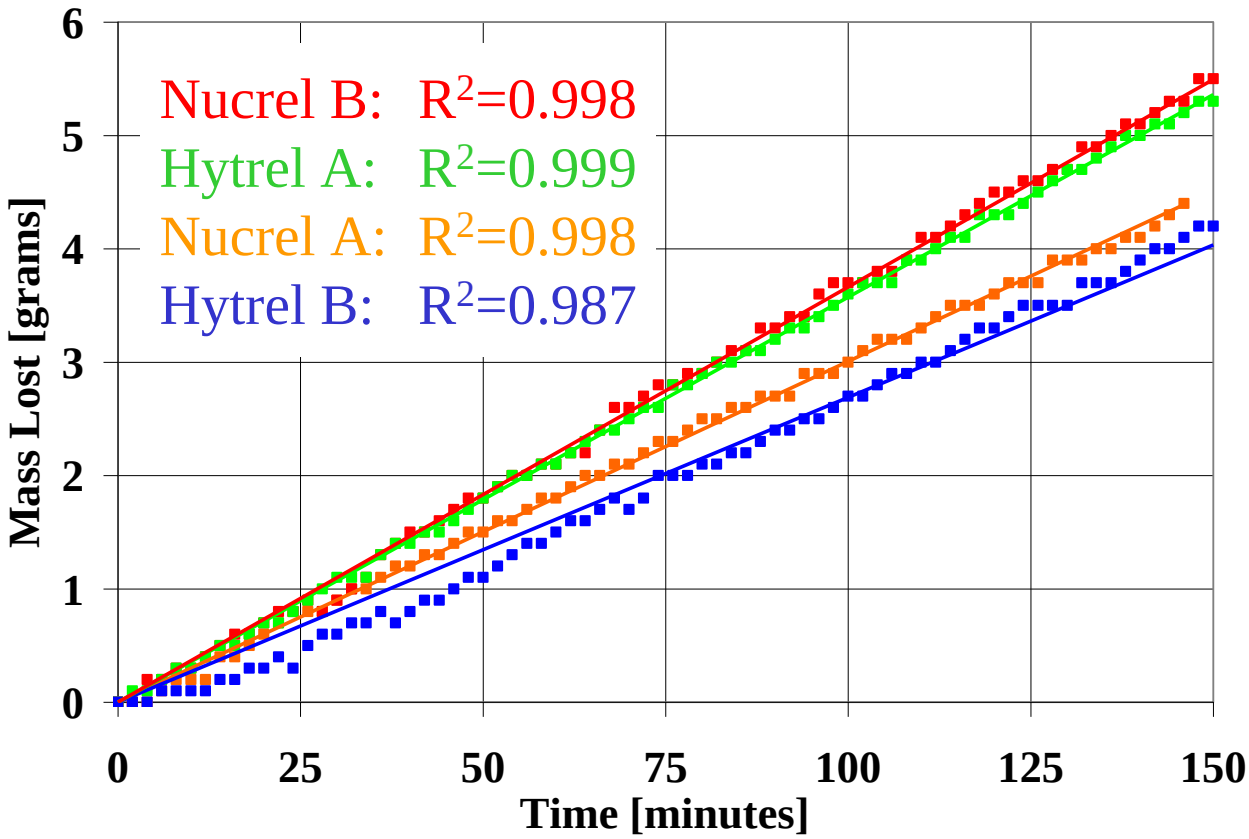

Figure 2: Mass time-rate-of-change for the evaporation apparatus under stead-state conditions confirm the linear mass flux rate through the membranes under study.

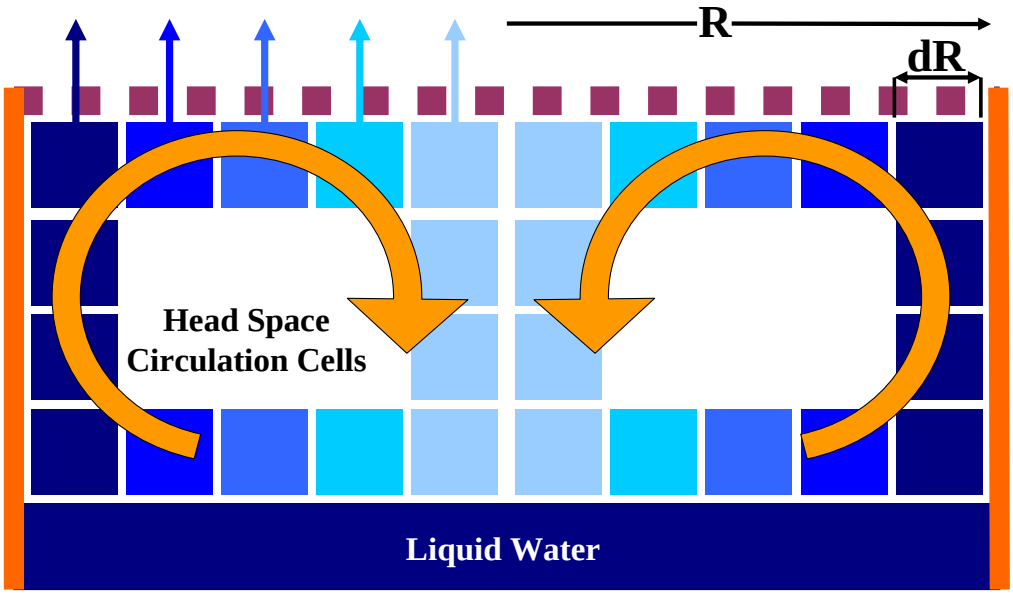

Figure 3: The radial concentration gradient across the membrane's upstream face results from diffusion through the membrane reducing the water mass concentration of a characteristic fluid element as it convects along the membrane surface.

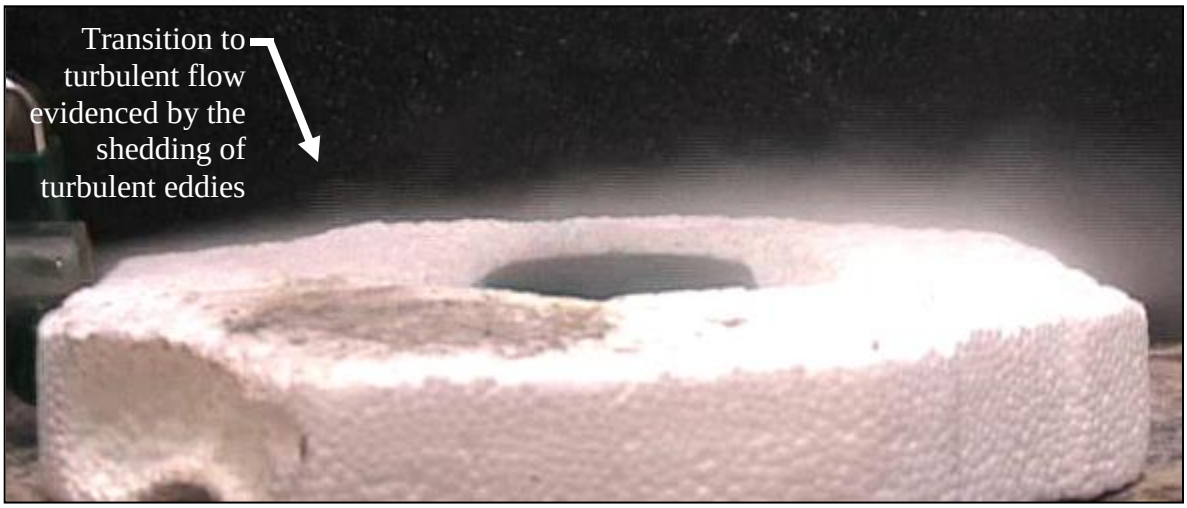

Figure 4: Transition to turbulence in the dry nitrogen jet flowing over the apparatus is observed to occur in advance of the membrane via a tracer mixed with the flow.

Table 1: A summary of parameters significant to the heat- and mass-transfer balance for the four FOEMs; with diffusion enabled, the heat balance converges to better than 12.4 percent.

Overlay [ ]	Input Power [watts]	Input Power Density [watts/m^2]	Δm/Δt [g/s]	Sensible Heat Transport [w]	Latent Heat Transport [w]	Heat Balance Error [%]
Nucrel A	7.60	1357	5.02E-04	5.48	1.18	12.4
Nucrel B	7.59	1355	6.05E-04	5.92	1.40	3.5
Hytrel A	7.65	1366	5.78E-04	5.88	1.36	5.4
Hytrel B	7.46	1333	4.67E-04	5.66	1.09	9.6

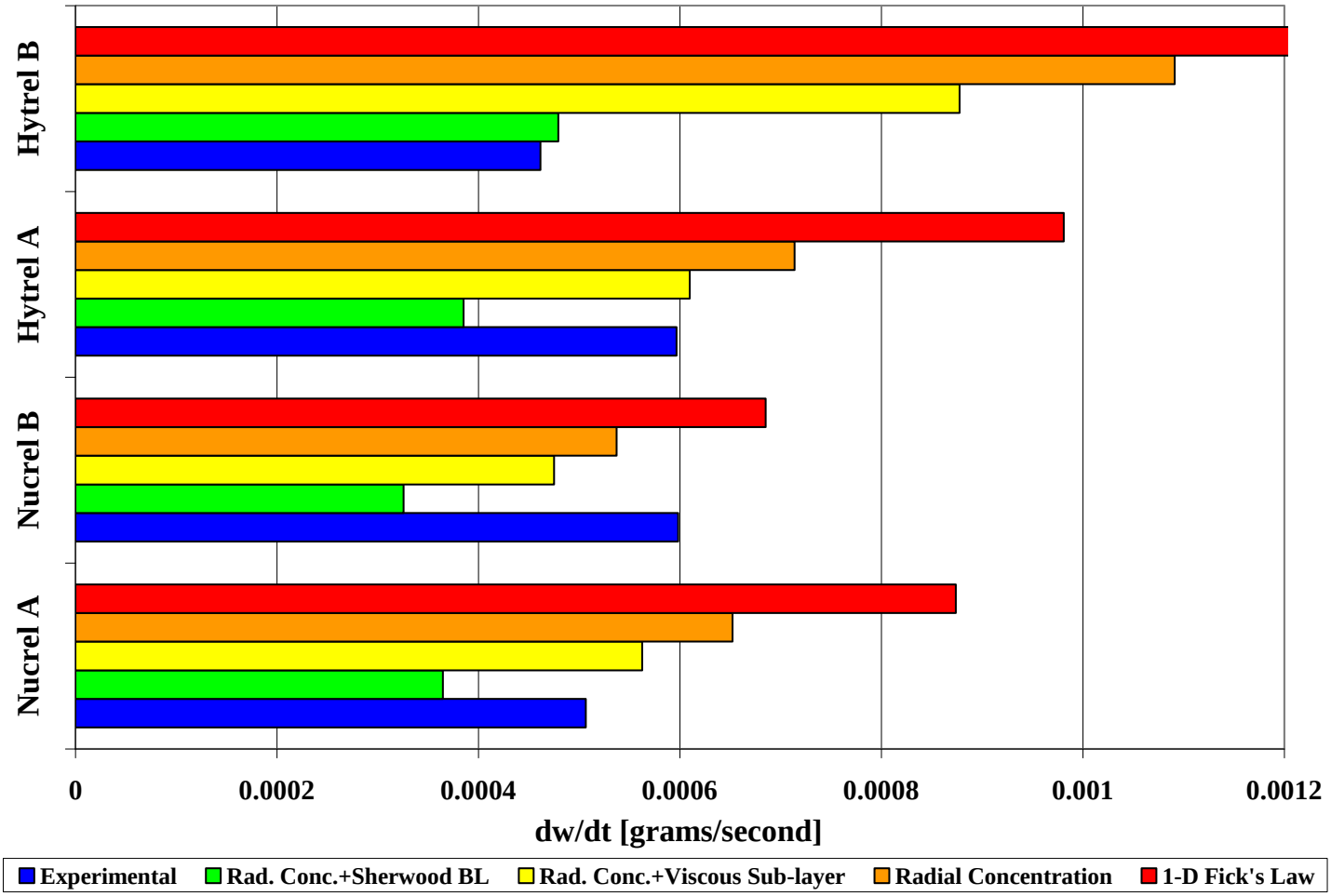

Figure 5: Results for all diffusion mass-transfer models are compared here with experimentally-measured flux rates for each FOEM case. Models combining radial concentration gradient with boundary layer diffusion resistance provide relatively good mass flux rate predictions.

Table 2: Parameters significant to the derivation of Bowen ratios for each experimental case indicate that one tenth to one quarter of the thermal energy transferred through the FOEMs was carried as latent heat.

Overlay	Porosity	Thermal Conductivity	Ave. T_{memtop}	Ave. T_{membot}	Ave. ρ_{memtop}	Ave. ρ_{membot}	$D_{H2O,air}$	B
[ ]	[ ]	[w/m-K]	[^oC]	[^oC]	[kg/m^3]	[kg/m^3]	[m^2/s]	[ ]
Nucrel A	0.0623	0.24	302.72	316.10	0	0.097	2.53E-05	8.7
Nucrel B	0.0548	0.24	301.95	314.99	0	0.098	2.51E-05	9.6
Hytrel A	0.0703	0.24	302.09	313.32	0	0.098	2.50E-05	6.5
Hytrel B	0.1454	0.24	305.76	314.65	0	0.098	2.54E-05	2.4

References

[i] M. J. Traum, P. Griffith, E. L. Thomas, and W. A. Peters, "Evaporative Cooling of Surfaces by Nano-engineered Membranes", ASME Journal of Heat Transfer (submitted)

[ii] Jang, J., Ullal, C.K., Choi, T., Lemieux. M.C., Tsukruk, V.V., and Thomas, E.L., 2006, "3D Polymer Microframes that exploit Length-Scale Dependent Mechanical Behavior", submitted to Advanced Materials.

[iii] M. J. Traum, P. Griffith, E. L. Thomas, and W. A. Peters, "Evaporative Cooling of Surfaces by Nano-engineered Membranes", ASME Journal of Heat Transfer (submitted)

[iv] Deen, W. M., 1998, Analysis of Transport Phenomena, Oxford University Press, New York, NY, pp. 487-493.

[v] Ibid.

[vi] Mills, A.F., Basic Heat & Mass Transfer, 2nd Ed., page 958

[vii] Mills, A. F., 1999, Basic Heat Transfer, 2nd Edition, Prentice Hall, Inc. Upper Saddle River, NJ, pp. 377-383.

[viii] Ibid.

[ix] M. J. Traum, P. Griffith, E. L. Thomas, and W. A. Peters, "Evaporative Cooling of Surfaces by Nano-engineered Membranes", ASME Journal of Heat Transfer (submitted)

[x] Mills, A. F., 1999, Basic Heat & Mass Transfer, 2nd Edition, Prentice Hall, Inc. Upper Saddle River, NJ, page 947.

[xi] Deen, W. M., 1998, Analysis of Transport Phenomena, Oxford University Press, New York, NY, page 12.

[xii] Cravalho, E.G., and Smith, Jr., J.L., 1981, Engineering Thermodynamics, Pitman Publishing Inc., Marshfield, MA, page 522.

[xiii] Deen, W. M., 1998, Analysis of Transport Phenomena, Oxford University Press, New York, NY, pp. 493-497.

[xiv] Turner, J.S., 1973, Buoyancy Effects in Fluids, Cambridge University Press, Cambridge, UK, pp. 222-225.

[xv] [11] Mills, A. F., 1999, Basic Heat & Mass Transfer, 2nd Edition, Prentice Hall, Inc. Upper Saddle River, NJ, page 281.

[xvi] Tritton, D.J., 1977, Physical Fluid Dynamics, Van Nostrand Company, Ltd., Wokingham, England, pp 275 – 281.

[xvii] Schlichting, H., Boundary Layer Theory 7th Ed., McGraw-Hill, Inc., pp. 623-626, 1979.

[xviii] Mills, A. F., 1999, Basic Heat Transfer, 2nd Edition, Prentice Hall, Inc. Upper Saddle River, NJ, pp. 314-316.

[xix] Mills

[xx] McCullough, E.A., Kwon, M., and Shim, H., 2003, "A comparison of standard methods for measuring water vapor permeability of fabrics", Measurement Science and Technology, 14, pp. 1402–1408, 2003.

[xxi] M. J. Traum, P. Griffith, E. L. Thomas, and W. A. Peters, "Evaporative Cooling of Surfaces by Nano-engineered Membranes", ASME Journal of Heat Transfer (submitted)

[xxii] Nellis, et al., "Updated Assessment of Microclimate Cooling Options for the Individual Soldier" technical report to the Army, February 2003.

[xxiii] "Desert Animals – Physiological Problems of Heat and Water" By Knut Schmidt-Nielsen, 1979

[xxiv] Drew W. Johnson, Cenk Yavuzturk, Justin Pruis, "Analysis of heat and mass transfer phenomena in hollow fiber membranes used for evaporative cooling", *Journal of Membrane Science,* Vol. 227, pp 159–171, 2003.

[xxv] Lewis, J.M., "The Story behind the Bowen Ratio", *Bulletin of the American Meteorological Society,* Vol. 76, No. 12, pp. 2433–2443, 1995.

Latent Heat Fluxes Through Nano-engineered Porous Materials

Matthew J. Traum[1,2], Peter Griffith[2], Edwin L. Thomas[1,3], William A. Peters[1]

[1]Institute for Soldier Nanotechnologies, Massachusetts Institute of Technology, [2]Department of Mechanical Engineering, MIT, [3]Department of Material Science and Engineering, MIT

Abstract: Transport of high-latent-heat-content vapors through pores in soft materials gives rise to energy fluxes without, or even opposed to, temperature gradients. Thermal management in nano-structures, MEMS, and larger systems, e.g., protective clothing, are potential applications. Exploiting these opportunities requires quantitative understanding of vapor transport within porous structures at realistic heat loads, including size-related effects of smaller pores (10-10,000 nm) e.g., rarefaction and surface curvature. This paper presents measured rates of water vapor transport across fiber-on-end membranes of Nucrel® (and Hytrel®) of thickness 113-126 μm (113-123 μm), with straight through pores of diameter 1.2-1.4 μm (8.4-14.1 μm), and average overall porosity of 6% (11%). Thermal buoyancy was induced within a 2.86 cm ID, 14.8 cm^3 capacity cylindrical evaporation chamber by controlled heating of liquid water from below at 1400 ± 70 W/m^2 (to mimic a typical daytime solar and metabolic heat load on desert soldiers). Natural convection delivered water vapor at known partial pressures in air to the upstream face of each membrane. Steady state rates of water vapor transport through the membrane to a zero-humidity cross flow of nitrogen (V = 2.8 m/s) were quantified by continuously weighing the entire apparatus. An apparatus-independent mass transfer resistance for each membrane was deduced by correcting the measured vapor fluxes for upstream and downstream boundary layer resistances including radial variations in vapor concentration at the membrane entrance. The apparatus-independent mass transfer resistances were then compared to predictions for Fickian diffusion with and without corrections for tortuosity and Knudsen diffusion.

Motivation:

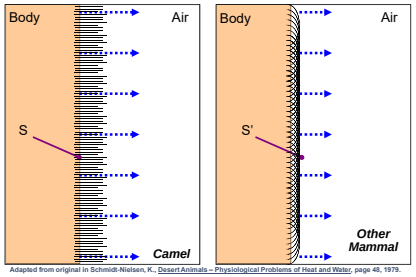

Adapted from original in Schmidt-Nielsen, K., Desert Animals – Physiological Problems of Heat and Water, page 48, 1979.

Camel fur (left) allows evaporation directly from the skin's surface (S) while providing thermal insulation, enabling lower skin temperature. For other mammals, skin temperature is higher because their fur (right) mats to their skin, wicking water to the surface (S') from where it evaporates.

Predicted steady-state armor temperature profiles

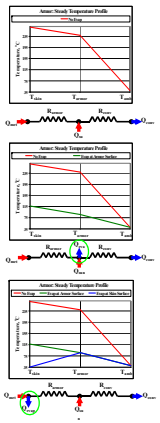

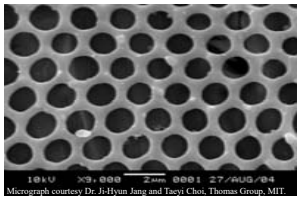

Micrograph courtesy Dr. Ji-Hyun Jang and Taeyi Choi, Thomas Group, MIT.

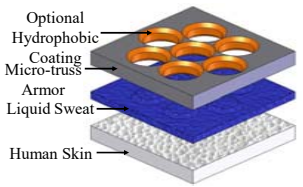

Nano-engineered Micro-truss combines camel-like water and thermal management with potential for ballistic protection.

Structure of Micro-truss Simulants:

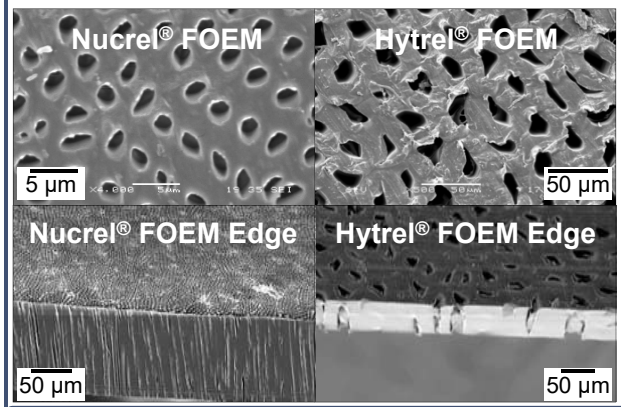

Membrane Size and Geometric Properties Important for Latent Heat Exchange

Material	Membrane Thickness [μm]	Membrane Porosity [%]	Average Pore Area [μm²]	Effective Pore Diameter [μm]
Nucrel A	112 ± 3	6.2 ± 0.9	1.7 ± 0.1	1.5 ± 0.1
Nucrel B	126 ± 2	5.5 ± 1.3	1.2 ± 0.4	1.2 ± 0.3
Hytrel A	113 ± 4	7.0 ± 1.4	56.7 ± 8.5	8.5 ± 0.8
Hytrel B	123 ± 2	14.5 ± 1.1	156 ± 13	14.1 ± 0.4
Latex	141 ± 6	0	N/A	N/A

Experimental:

Decouple latent from sensible heat transfer by accounting for apparatus parameters:
- **Thermal buoyancy in the liquid water**
- **Thermal buoyancy in the air head space**
- **Upstream-boundary-layer radial concentration gradient**
- **Downstream boundary layer transport resistance.**

Measured mass fluxes at steady state, disaggregated from apparatus effects, give apparatus-independent membrane transport resistance.

$$\frac{\dot{m}}{A} = \frac{\rho_2 - \rho_3}{R_{BL,2} + R_{mem} + R_{BL,3}}$$

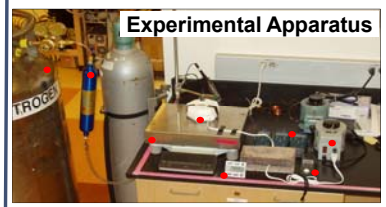

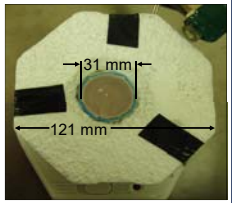

Heat Balance Closure to +3.5% - 12.4%

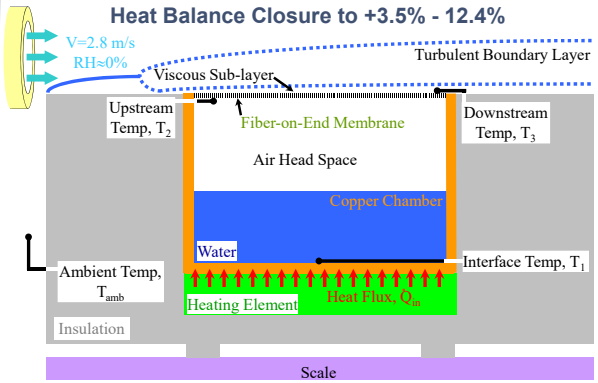

Results and Analysis:

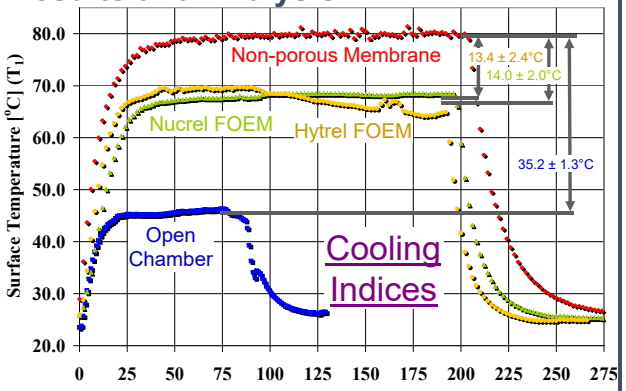

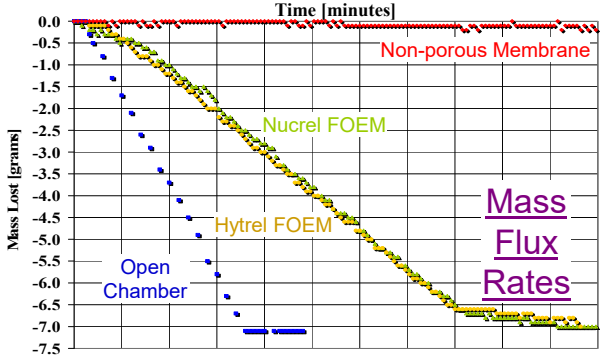

Summary and Conclusions:

- **Validated apparatus to quantify latent heat and vapor mass transport through nano-engineered porous materials under realistic heat load, temperature, and environmental conditions**
- **Demonstrated appreciable cooling of surfaces by water evaporation through nano-engineered overlays, despite low porosity (5-15%) and tiny pore diameters (1.2 – 14.1 μm)**
- **Knudsen effects minor (< 8%) on latent heat transmission for the above materials, pore IDs, and operating conditions**
- **Further research, in progress at the ISN, is needed to assess "deep nano scale" effects, e.g., of 50-500 nm ID pores**
- **By metering the magnitude and direction of latent heat flows, nano-engineered materials have potential to:**

-integrate cooling (or heating) with high mechanical strength for blast or ballistic protection of people and hardware;

-transmit energy without or against thermal gradients, e.g., to power heat engines or neutralize adverse heat fluxes

Acknowledgements: This research was supported by the U.S. Army through the Institute for Soldier Nanotechnologies, under Contract DAAD-19-02-D-0002 with the U.S. Army Research Office. The content does not necessarily reflect the position of the Government, and no official endorsement should be inferred. We thank Drs. Vivek Kapur and Wayne Marsh of DuPont for supplying samples of their FOEM membranes. Hytrel® and Nucrel® are registered trademarks of the I. E. DuPont de Nemours Company.